Chemical Engineering Journal 476 (2023) 146877

Contents lists available at ScienceDirect

Chemical Engineering Journal

journal homepage: www.elsevier.com/locate/cej

Solar-driven photodegradation of ciprofloxacin and *E. coli* growth inhibition using a Tm^{3+} upconverting nanoparticle-based polymer composite

Siyuan Fan [a], Jabez Ebenezer Inkumsah Jnr [a], Enrico Trave [b], Matteo Gigli [b], Tanmaya Joshi [a,*], Nadia Licciardello [a], Massimo Sgarzi [b,*], Gianaurelio Cuniberti [a,*]

[a] Institute for Materials Science, Max Bergmann Centre for Biomaterials and Dresden Center for Nanoanalysis, TU Dresden, D-01062 Dresden, Germany
[b] Department of Molecular Sciences and Nanosystems, Ca' Foscari University of Venice, Via Torino 155, I-30172 Venezia Mestre, Italy

ARTICLE INFO

Keywords:
Solar-driven photocatalysis
Upconverting nanoparticles
Photosensitive polymer
Nanocomposite
Antibiotics
Antimicrobial
Wastewater

ABSTRACT

Solar-driven photocatalysis is of great interest in terms of a sustainable use of energy and its application in wastewater treatment. The UV light-driven photogeneration of H_2O_2 by solar irradiation is an advanced strategy for the treatment of bacteria and recalcitrant pollutants in wastewater, but suffers from low efficiencies. In this work, a solar-driven multifunctional nanocomposite consisting of Tm^{3+} upconverting nanoparticles, poly(vinyl alcohol), poly(acrylic acid) and hydroxylated sulfonated poly(ether ether ketone) was prepared. The components were crosslinked via a heating treatment at 170 °C, resulting in a non-leaching porous material. This nanocomposite exhibited excellent adsorption ability (89 % in 150 min) toward a 100 mg/L ciprofloxacin aqueous solution and proved to photodegrade it (50 %) upon 4 h artificial solar irradiation, exploiting photon upconversion processes. Moreover, an 80 % bactericidal effect against *E. coli* was registered upon sunlight irradiation. Altogether, these results suggest the feasibility of a solar-driven wastewater treatment based on upconverting nanoparticles.

1. Introduction

Different techniques (primary, secondary and tertiary treatments) [1] have been used in conventional wastewater treatment to remove pollutants. Nevertheless, this process is not effective in removing persistent contaminants present in trace amounts, such as antibiotics [2]. In this context, photocatalysis, the most exploited among advanced oxidation processes (AOPs) [3–7], is regarded as a complementary technique to conventional systems. Unfortunately, photocatalysis makes use in most of the cases of UV-activatable nanoparticulate semiconductor materials such as TiO_2, which cannot operate efficiently under visible light irradiation, due to their wide bandgap (as for TiO_2, 3.0 eV for rutile phase and 3.2 eV for anatase phase) [8]. This represents a limit since only 5 % of the solar irradiance spectrum [9] is absorbed by these materials. Much research is thus devoted to the study of low bandgap materials, able to absorb visible light, which accounts for 45 % of solar photons [10–12]. Moreover, the recovery and reuse of these nanoparticles is cumbersome due to high costs and sophisticated equipment [13,14]. To overcome this limitation, the immobilization of these nanoparticles on solid supports has been investigated, which in turn suffers from limited effective surface area for contaminant adsorption and secondary pollution caused by leaching of nanoparticles from the support materials [15]. In this context, photosensitive polymers have received considerable attention, due to the high number of photoinitiating unit per chain, which yields higher degradation efficiencies[16].

Lockhart *et al.* [17] and Little *et al.* [18] previously reported the formation of H_2O_2 in air-saturated aqueous solutions by a photosensitive polymer blend composed of sulfonated poly(ether ether ketone) (SPEEK) and PVA upon irradiation with 350 nm photons. H_2O_2 is a well-known active ingredient for the degradation of pollutants [19] and exhibits effective bactericidal properties against microorganisms [20]. Nevertheless, this photosensitive blend can only operate under UV light irradiation [17].

The strategy proposed in this paper to overcome the use of UV light for the operation of these photosensitive polymers is to couple them with lanthanide-based upconverting nanoparticles (UCNPs), which have the ability to convert NIR light into UV or visible photons [21], with the aim

* Corresponding authors.
E-mail addresses: tanmayamonash@gmail.com (T. Joshi), massimo.sgarzi@unive.it (M. Sgarzi), gianaurelio.cuniberti@tu-dresden.de (G. Cuniberti).

https://doi.org/10.1016/j.cej.2023.146877
Received 21 July 2023; Received in revised form 9 October 2023; Accepted 22 October 2023
Available online 24 October 2023

of creating a multifunctional nanocomposite operable under solar irradiation [22,23]. The introduction of UCNPs in the formulation is necessary to endow the proposed material with the ability of absorbing NIR light and of converting it into energy in the UV range, which is subsequently transferred to sensitise the excitation of the polymer matrix, whose reaction with oxygen ultimately yields H_2O_2. In the absence of UCNPs, the prepared polymer matrix would be able to absorb exclusively UV light. The presence of the nanoparticles is expected to allow the use of solar light as an excitation source, which represents an advantage in terms of sustainability of the overall water remediation process.

Herein, we prepared poly(acrylic acid)-derivatized β-$NaYF_4$:Yb^{3+} (20 %), Tm^{3+}(2 %) UCNPs covalently bound to a PVA/hydroxylated SPEEK photosensitive polymer matrix and tested the ability of this polymer nanocomposite of producing H_2O_2 under artificial and real solar irradiation. Moreover, the adsorption capacity and the photodegradation ability of this material towards the antibiotic ciprofloxacin were studied, together with its antibacterial activity against *E. coli*.

2. Materials and methods

2.1. Chemicals

Poly(ether ether ketone) (PEEK, 450 PF) was purchased from Victrex and used for the synthesis of sulfonated poly ether ether ketone (SPEEK).

Poly(acrylic acid) sodium salt (molecular weight 5100 g/mol), ciprofloxacin (CIP), sodium borohydride ($NaBH_4$), yttrium(III) chloride hexahydrate (99.99%), ytterbium(III) chloride hexahydrate (99.99%), thulium(III) chloride hexahydrate (99.99%), ammonium fluoride (ACS reagent 98.0%), sodium oleate (99.0%) and oleic acid (technical grade 90%) were obtained from Sigma-Aldrich. Dimethylsulfoxide (DMSO) (≥99,5%) was purchased from Merck. Poly(vinyl alcohol) (PVA, 98–99% hydrolyzed, molecular weight 85000 g/mol) was purchased from ThermoFisher GmbH. Therminol® 66 (T66) was obtained from FRAGOL GmbH (Mülheim, Germany, product number: 2600267). Luria-Bertani (LB) broth was purchased from Sigma-Aldrich. *E. coli* YFP, MG1655 galK: SYFP2-FRT was used for antibacterial tests. All other chemicals and organic solvents were of analytical grade. All solutions and suspensions were prepared with ultrapure water produced by a MembraPure Astacus system (MembraPure GmbH, Hennigsdorf, Germany).

2.2. Preparation of SPEEK

SPEEK was synthesized by sulfonation of PEEK following the procedure described previously [24]. 10 g PEEK were gradually added to a beaker containing 100 mL concentrated H_2SO_4 (>95 %) under constant mechanical stirring using a HT-120DX overhead stirrer (Witeg Labortechnik GmbH, Wertheim, Germany). The beaker was heated to 75 °C and kept at this temperature for 24 h in an oil bath.

The reaction was terminated by precipitating the polymer solution into a large excess of ice-cold ultrapure water. 10 mL of 6 M NaOH aqueous solution was then dropped gradually to neutralize the excess H_2SO_4 until pH 6–7 was reached. The SPEEK was finally dried in a ventilated oven at 60 °C for 24 h.

2.3. Preparation of hydroxylated SPEEK (SPOH)

The obtained SPEEK was hydroxylated by using the procedure described previously [25]: DMSO (9 mL) and $NaBH_4$ (10 mg) were introduced into a 50 mL round bottom flask combined with a reflux condenser. The solution was heated at 120 °C under stirring. After the addition of SPEEK (900 mg), the reaction was stirred for 12 h at 120 °C in an oil bath. After the reaction was terminated by letting it cool to room temperature, 2 mL methanol were added and the mixture was stirred for another 2 h. The obtained solution was then casted on a Petri dish and dried in ventilated oven at 70 °C for 5 h. Hydroxylated SPEEK (SPOH) was thus obtained.

2.4. Synthesis of oleate (OA) coated upconverting nanoparticles (OA-UCNPs)

Thulium-doped UCNPs (β-$NaYF_4$:Yb^{3+}/Tm^{3+}(20/2%)) were synthesized following the procedures described previously [26,27] making use of a Schlenk line. The powders of YCl_3 (0.78 mmol), $YbCl_3$ (0.2 mmol) and $TmCl_3$ (0.02 mmol) were added to the mixture of oleic acid (8 mL) and Therminol® 66 (12 mL) and heated to 120 °C under vacuum for 60 min. Afterwards, the temperature of the reaction solution was decreased to 90 °C with an argon stream.

NH_4F (4 mmol) and sodium oleate (2.5 mmol) were added to this solution and stirred for 30 min under argon. Thereafter, the mixture was maintained at 320 °C under argon and stirred for 1 h. After cooling, Tm-doped UCNPs were collected by precipitation in ethanol and isolated by centrifugation (2383×*g*, 10 min). The supernatant was removed, and the white pellet was washed three times by suspension in a minimal amount of hexane and precipitated again in ethanol by centrifugation (2383×*g*, 10 min). Subsequently, the obtained oleate-capped UCNPs were resuspended in hexane and stored at 4 °C until further use.

2.5. Preparation of PAA-UCNPs

The surface of the obtained oleate-capped UCNPs was decorated with polyacrylic acid (PAA) according to the previously described procedure [26,28]. 3 mL of the oleate-capped UCNPs stock suspension in hexane (10 mg mL^{-1}) were vigorously stirred with $NOBF_4$ (30 mg) in DMF (3 mL) for 10 min at room temperature. The BF_4^--coated nanoparticles were obtained in the lower DMF phase. The precipitation of BF_4^--coated UCNPs was performed adding chloroform (2 × 20 mL) followed by centrifugation (2383 × *g*, 15 min). The collected UCNPs were dissolved in 2 mL DMF and centrifuged (1000 × *g*, 3 min) to remove any larger aggregates.

Subsequently, the as-prepared suspension of BF_4^--coated UCNPs (30 mg in 2 mL DMF) was gradually added to a solution of the PAA ligand (30 mg) in water (2 mL) and mixed for 20 min. The particles were gathered from the mixture by centrifugation (21000 × *g*, 30 min) and washed twice to remove the excess of PAA ligands. Aggregates were eliminated by means of centrifugation (1000 × *g*, 3 min) and the supernatant was stored at 4 °C.

2.6. Synthesis of PAA-UCNP-embedded PVA/SPOH-PAA nanocomposite

The synthesis of the PAA-UCNP-embedded PVA/SPOH-PAA nanocomposite was performed following the procedure described previously [29,30] with addition of PAA-UCNPs. The weight ratio of SPOH/PVA used in the preparation of the film was 30:70 (225 mg of SPOH and 525 mg of PVA). First, the two polymers were separately dissolved in 10 mL of water under magnetic stirring. The SPOH solution was placed in an oil bath at 50 °C for 1 h while the PVA solution was heated at 100 °C in an oil bath for 1 h. To prevent water evaporation, the PVA solution was heated under reflux while the SPOH solution was covered with Parafilm. The two solutions were subsequently mixed together at 60 °C for 1 h, yielding a 30:70 wt% SPOH:PVA mixture (20 mL). Afterwards, an aqueous suspension of PAA-UCNPs (33.3 μL from 30 mg/mL stock suspension) was added to the SPOH:PVA mixture and stirred for 1 h. PAA (6 mL of a 5 wt% aqueous solution) was added to the mixture, which was subsequently poured into a Petri dish and dried in oven at 60 °C for 5 h. This step was followed by the crosslinking heating treatment at 170 °C for 30 min, which yielded the formation of ester bonds between the carboxylic groups of PAA and the hydroxyl groups of PVA and SPOH.

2.7. Characterization of UCNPs and of the nanocomposite

The quantification of Y, Yb and Tm in the UCNP samples was performed by inductively coupled plasma mass spectrometry (ICP-MS) with iCap RQ instrument (Thermo Fisher Scientific, Waltham, Massachusetts, USA).

The morphology and size of UCNPs were assessed by Scanning Transmission electron microscope (STEM). The TEM images were obtained by using a 200 kV TEM microscope JEOL JEM F200C. The size distribution of the UCNPs from TEM images were processed by ImageJ software (National Institute of Health, USA), which was used to calculate the average diameter of 150 particles. The hydrodynamic diameters and colloidal stability of the UCNPs were analysed by means of a Malvern Zetasizer Nano ZS DLS instrument (Malvern Panalytical Ltd, Malvern, United Kingdom). All measurements were processed at 25 °C.

The photoluminescence properties of UCNPs and of the nanocomposite were measured with a FluoroLog 3–21 system (Horiba JobinYvon) equipped with a 980 nm laser diode (CNI, model MDL-III-980) as excitation source (output power of 2 W, power density of 5 $W{\cdot}cm^{-2}$). The detection system was composed of an iHR300 single grating monochromator coupled to a R928 Hamamatsu PMT.

Attenuated Total Reflectance-Fourier Transform Infrared (ATR-FTIR) spectroscopy was used for the compositional analysis of UCNPs and of the nanocomposite. ATR-FTIR spectra were registered on IRAffinity-1S (Shimadzu, Kyoto, Japan) equipped with a GladiATR-10 ATR accessory. The spectra were obtained in absorbance mode, registering 32 scans with a resolution of 2 cm^{-1} in the wavenumber range 4000–500 cm^{-1}.

The morphology of the nanocomposite was determined by means of a scanning electron microscope (SEM) equipped with microscope Zeiss Gemini SEM 500 by using InLens mode and ESB mode.

Thermogravimetric analysis (TGA) was carried out by means of a Perkin Elmer TGA 4000 to investigate the nanocomposite thermal stability under 20 $mL{\bullet}min^{-1}$ N_2 flow from 30 to 800 °C with a heating rate of 10 °C•min^{-1}. Differential Scanning Calorimetry (DSC) analysis was performed using a Mettler Toledo DSC in the range 30–220 °C with a heating/cooling rate of 20 °C•min^{-1} under a 40 $mL{\bullet}min^{-1}$ N_2 atmosphere. The instrument temperature was calibrated using indium as standard.

Contact angle measurements were performed by means of a First Ten Ångstroms FTA1000 Drop Shape instrument, depositing 1 μL droplets of ultrapure water on different spots of the nanocomposite at 25 °C. The water contact angle was measured immediately after the drop deposition and every 30 s.

2.8. Swelling experiments

The water absorption ability of the nanocomposite was investigated by means of swelling tests in water. The dry films (ca. 650 mg) were immersed in 200 mL ultrapure water at room temperature [17]. The swelled samples were weighed at defined time points: 0, 5, 10, 15, 30, 45, 60, 90, 120 min, until reaching a constant weight.

The swelling capacity was determined using the following equation:

$$Swelling\ capacity\ (\%) = \frac{W_s - W_d}{W_d} \cdot 100 \quad (1)$$

where W_d is the weight of the dried nanocomposite and W_s is the weight of the swelled sample recorded when a constant weight was reached.

2.9. Hydrogen peroxide generation ability tests

UV and artificial solar light sources were used to assess the ability of the nanocomposite to produce H_2O_2 upon irradiation. As for the tests under UV light, a UV irradiator equipped with 5 UV lamps (Philips, TL 8 W BLB 1FM/10X25CC, $\lambda_{em,max}$ = 365 nm) was used, whose measured irradiance at the level of the reactor was ~ 18.6 $W{\cdot}m^{-2}$. As for the irradiation with artificial solar light, an artificial lamp (Ingenieurbüro Mencke & Tegtmeyer GmbH, Germany; 98 $W{\cdot}m^{-2}$ irradiance) was used, equipped with a silicon irradiance sensor controlled by Susicontrol software (version 2.9.0). The wavelength range of the artificial lamp spanned from 400 to 1100 nm according to the report of the supplier.

Each swelled film was completely immersed in ultrapure water and irradiated. Every experiment was performed three times under constant magnetic stirring. Supernatant aliquots of 1 mL were withdrawn at defined time points (0, 5, 10, 15, 30, 45, 60, 90, 120 min). According to the iodide-molybdate method [17,18], each aliquot was mixed with 1 mL 0.1 M potassium biphthalate aqueous solution and 1 mL of a mixture containing 0.4 M KI, 0.06 M NaOH and $2{\cdot}10^{-4}$ M $(Na)_2MoO_4$, resulting in a 3 mL total final volume. The mixture was transferred into a 1 cm-optical path quartz cuvette and analysed by means of a Cary 100 UV–Vis spectrophotometer (Santa Clara, CA, USA).

The quantification of the produced hydrogen peroxide was thus performed following the reaction:

$$3I^- + H_2O_2 + 2H^+ \rightarrow I_3^- + 2H_2O \quad (2)$$

and registering the absorption band of I_3^- at 350 nm. The concentration of I_3^- was calculated by means of Lambert-Beer law.

2.10. Adsorption and photocatalytic activity tests

First, the adsorption tests were conducted immersing the swelled films completely in 100 mL of 100 $mg{\cdot}L^{-1}$ CIP solution at pH 6.5 under constant stirring and maintaining the system in dark conditions. Supernatant aliquots of 1 mL were withdrawn at defined time points (0, 5, 10, 15, 30, 45, 60, 90, 120, 150 min). The variations of the concentration of CIP in the supernatant were followed by means of UV–Vis spectroscopy, considering the absorption maximum at 272 nm. The adsorption–desorption equilibrium was reached after 150 min.

Subsequently, the photocatalytic activity tests were performed using the same artificial lamp used for the hydrogen peroxide generation ability tests with the same experimental conditions.

Supernatant aliquots of 1 mL were withdrawn at defined time points (0, 5, 10, 15, 30, 45, 60, 90, 120, 180, 240 min) and the concentration of CIP was assessed by means of UV–vis spectroscopy.

2.11. Leaching experiments

The leaching of UCNPs from the film was determined by inductively coupled plasma mass spectrometry (ICP-MS) with iCap RQ instrument (Thermo Fisher Scientific, Waltham, Massachusetts, USA).

The nanocomposite was immersed in ultrapure water at room temperature and constant stirring. Aliquots of the supernatant were withdrawn for the ICP-MS analysis after 24 h, 48 h, 72 h, 1 week, 2 weeks, 3 weeks and 4 weeks.

The percentage of entrapped UCNPs was calculated using the following equation:

$$Entrapped\ UCNPs\ \left(\%\right) = \left(m_{total} - \frac{m_{ICP-MS}}{V_{aliquot}} \cdot V_{total}\right) \cdot 100 \quad (3)$$

m_{total}: total amount of UCNPs contained in the sample.

m_{ICP-MS}: amount of UCNPs detected via ICP-MS contained in the supernatant aliquot.

$V_{aliquot}$: volume of the aliquot.

V_{total}: total volume of the supernatant.

The leaching of SPEEK and PVA from the films was determined by means of a Cary 100 UV–Vis spectrophotometer (Santa Clara, CA, USA). The film was immersed in water in dark conditions under constant stirring and aliquots of the supernatant were withdrawn for UV–vis analysis after 0, 5, 10, 15, 30, 45 and 60 min and 24 h.

2.12. Reusability tests

After the adsorption and photocatalytic experiments, the nanocomposite was regenerated by desorption of CIP [31], which was conducted by soaking the film in 200 mL 70:30 ethanol: ultrapure water mixture under constant stirring for 6 h at 50 °C on an oil bath.

Subsequently, the recovered film was utilized for a new cycle of adsorption and photocatalytic experiments. Three cycles were performed in total.

2.13. Antibacterial tests

Laboratory supplies were sterilized by autoclaving at 121 °C and subsequently used in the experiments in a biosafety level 1 laboratory.

The *E. coli* suspension was cultivated using the following procedure: 12 g of LB broth were dissolved in 600 mL ultrapure water in a 1 L sterile bottle and subsequently autoclaved. After cooling to room temperature, 50 mL of sterile LB broth solution were transferred to a sterile flask and 2 mL *E. coli* culture were added under a laminar flow chamber. Subsequently, the suspension was incubated at 37 °C overnight. The concentration of *E. coli* suspension after cultivation was assessed by optical density measurements at 600 nm using a Biophotometer (Eppendorf, Hamburg, Germany).

The concentration of *E. coli* suspension was calculated as follows:

$$Conc.\ E.Coli = OD_{600} \cdot 8 \cdot 10^8 \frac{cells}{mL} \quad (4)$$

where OD_{600} is the value of optical density at 600 nm. The *E. coli* suspension was then stored at 4 °C as stock solution for further experiments.

First, the adsorption ability of nanocomposite was tested against *E. coli* in dark conditions. 8 mL of *E. coli* stock solution were diluted in 80 mL LB broth medium to obtain an optical density equal to ca. 0.05. The obtained solution was divided into four sterile flasks. These four suspensions were prepared for the following adsorption and bactericidal experiments. Two of the *E. coli* suspensions were kept in contact with 750 mg of polymer matrix and 750 mg of nanocomposite, respectively, in the absence of light for 60 min to reach the adsorption–desorption equilibrium. The *E. coli* suspension without film was used as a reference. All experiments were performed at room temperature. Aliquots of 1 mL were withdrawn at defined time points (0, 5, 10, 15, 30, 45, 60 min) and the concentration was monitored by using a Biophotometer (Eppendorf, Hamburg, Germany). The obtained data were the average of three replicated tests.

Subsequently, the bactericidal effect of the nanocomposite upon irradiation with sunlight was investigated as follows: the optical density of *E. coli* suspension was monitored over time up to 60 min in the absence of nanocomposite, in the presence of 750 mg of the polymer matrix and in the presence of 750 mg of nanocomposite, respectively, under sunlight irradiation (331.41 $W \cdot m^{-2}$ irradiance). The results were compared to the *E. coli* suspension in the absence of light. All experiments were performed at ambient temperature (20 °C). The bactericidal efficiency (*BE*) was calculated by using Eq. (6):

$$BE = \frac{OD_{dark} - OD_X}{OD_{dark}} \cdot 100 \quad (5)$$

where OD_{dark} is the OD_{600} of the reference sample at each time point in the absence of light, and OD_X is the OD_{600} of treated samples at the corresponding time point upon sunlight irradiation. X refers to three different experimental conditions: i) the absence of the nanocomposite, ii) the presence of the polymer matrix or iii) the presence of the nanocomposite.

The bactericidal kinetic rate constant k_{bact} (min^{-1}) of *E. coli* was assessed by using the following equation:

$$k_{bact} = \frac{OD_{dark} - OD_X}{t} \quad (6)$$

where OD_{dark} and OD_X refer to the same parameter of Eq. (5) and t is time (min).

Subsequently, 2 mL of the mixture were withdrawn from each sample and added to 20 mL LB broth medium. These diluted samples were cultivated at 37 °C for 5 h. The bactericidal effect of these samples was calculated taking the dark blank sample as a reference. Aliquots of 1 mL were withdrawn at defined time points (0, 60, 120, 180, 240, 300 min) and the concentration was monitored by using a Biophotometer (Eppendorf, Hamburg, Germany) to monitor the regrowth behavior of *E. coli* suspension.

3. Results and discussion

3.1. Preparation and characterization of the nanocomposite

Poly(acrylic acid) (PAA) was utilized as crosslinking agent to form an ester bond network with PVA and the hydroxylated SPEEK (SPOH) via a 30 min heating treatment at 170 °C. Concurrently, PAA was used as a ligand to decorate the UCNPs, thanks to the ability of carboxylate groups to stably coordinate lanthanide ions. Overall, the formation of the ester bond network originated from the crosslinking between the carboxylic groups of both PAA and PAA-UCNPs and the hydroxyl groups of PVA (Fig. 1).

The successful crosslinking reaction was proved via ATR-FTIR measurements. The spectrum of the nanocomposite (Fig. 2 *a*) presented the peaks at 1400 cm^{-1} and 1080 cm^{-1} attributable to asymmetric and symmetric stretching vibrations of the sulfonate functional group of SPOH. The peaks at 1748 cm^{-1}, 1225 cm^{-1} and 1123 cm^{-1} were respectively attributed to the C=O, C–C–O and O–C–C stretching vibrations of the ester groups formed via the crosslinking reaction. The peak at 1596 cm^{-1} accounted for the COO asymmetric stretching of the unreacted carboxylic groups of PAA, while the peak at 3280 cm^{-1} was attributed to the stretching vibrations of hydroxyl groups of PVA (*Fig. S10a*) and SPOH (*Fig. S3a*) [24,30,32], with the corresponding bending vibration at 1298 cm^{-1}.

Imbibition tests with water revealed a 90% swelling capacity which was reached in 60 min (*Fig. S4*). The same value was obtained for the polymer matrix in the absence of UCNPs, confirming that UCNPs did not have a detrimental effect on the swelling capacity of the system, which is fundamental for the continuous feed of O_2 dissolved in water for the production of H_2O_2.

ICP-MS measurements of water samples analyzed after a 24 h imbibition of the nanocomposite film indicated that more than 99% PAA-UCNPs remained entrapped (*Table S3*). The reticulation reaction endowed thus the nanocomposite with excellent anti-leaching properties, an important feature to avoid secondary pollution during operations in wastewater treatment.

SEM images of the nanocomposite film were registered after a 2 h imbibition period. These measurements revealed the high porosity of the nanocomposite film (Fig. 2 *b*), which exhibited pores in the micrometer range; BET analysis did not reveal the presence of micro-, meso- or macropores in the nanometric range (data not shown). Fig. 2 c shows the distribution of PAA-UCNPs in the film, where it was possible to observe aggregates of nanoparticles, probably formed at 170 °C during the crosslinking process.

Sessile drop measurements revealed a contact angle of (69 ± 2)°, which proves the hydrophilicity of the film. During these measurements, it was moreover possible to observe the drop being absorbed by the film over time and the film swelling as a result of water absorption.

TGA measurements (*Fig. S14*) revealed 4 weight losses centred respectively at 100 °C (weight loss 11 %), 346 °C (weight loss 45 %), 443 °C (weight loss 18 %) and 759 °C (weight loss 7 %). While the first weight loss at 100 °C is attributable to water, the one at 346 °C is the sum of the contributions of the degradation of PVA (elimination of OH groups) [33] and SPOH (degradation of $-SO_3H$ groups)[34,35], while

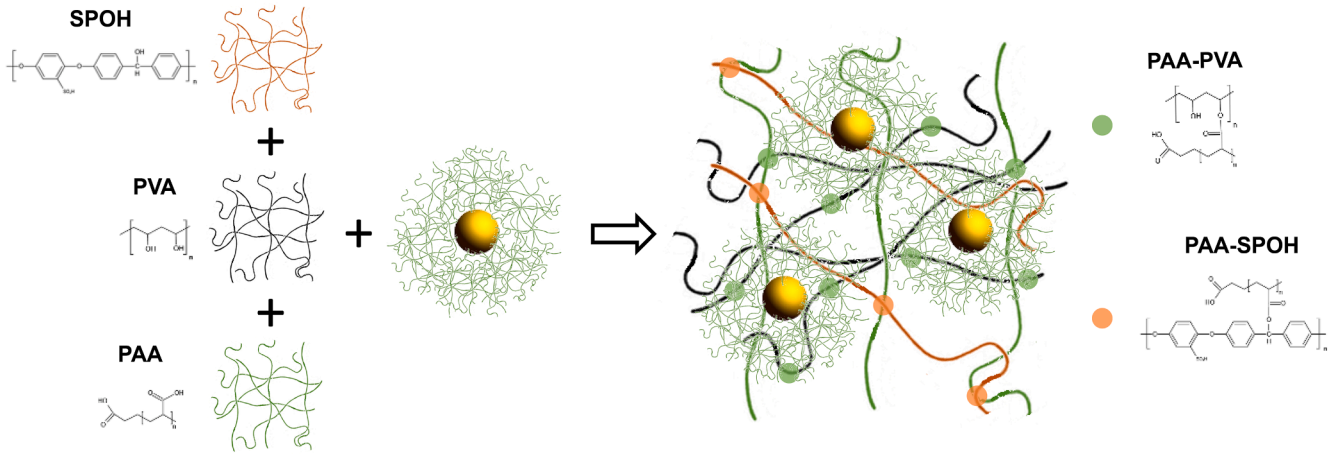

Fig. 1. Schematic preparation process of the PAA-UCNP-embedded PVA/SPOH-PAA nanocomposite (the yellow spheres represent PAA-decorated β-$NaYF_4$:Yb^{3+} (20%), Tm^{3+}(2%) UCNPs). (For interpretation of the references to colour in this figure legend, the reader is referred to the web version of this article.)

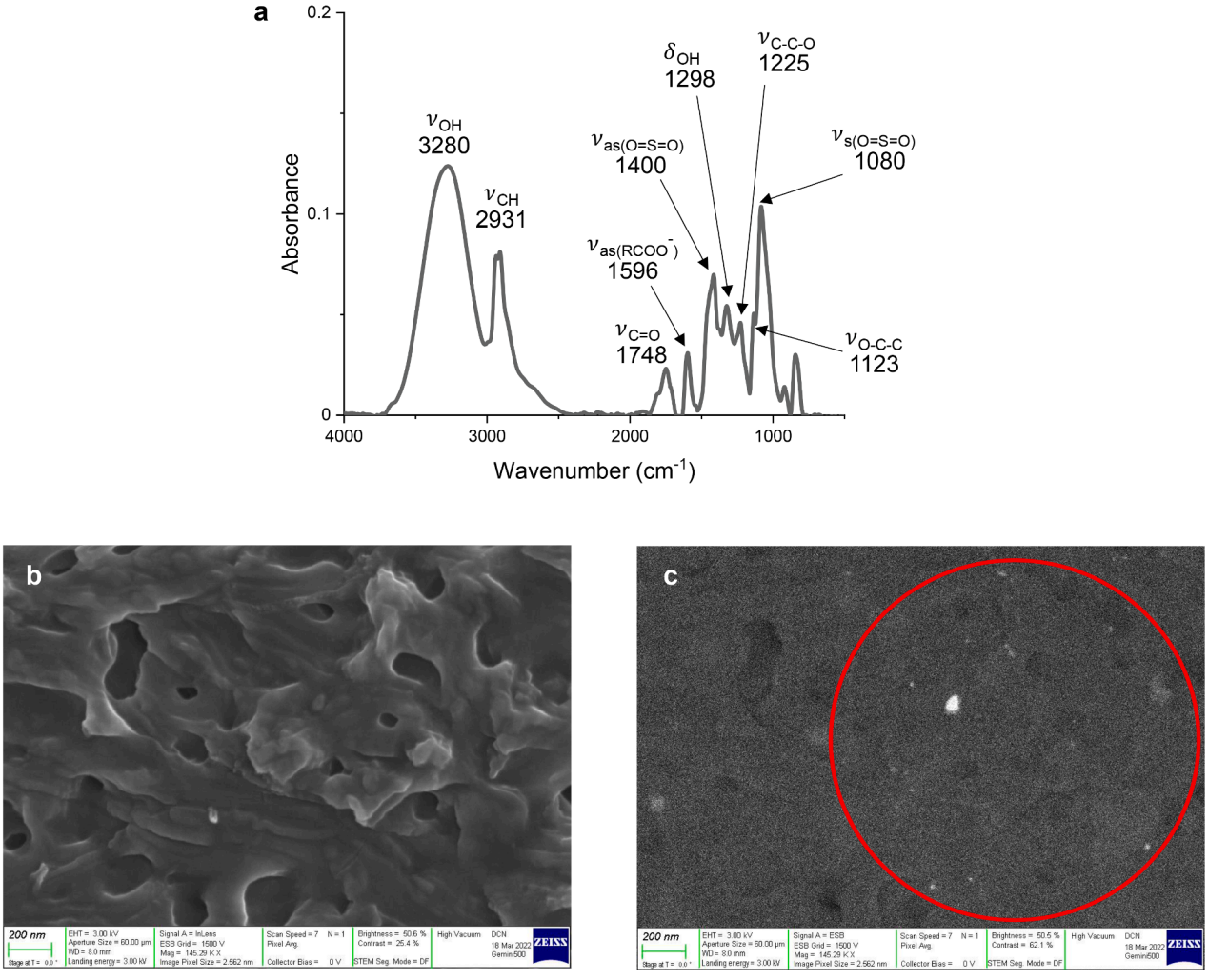

Fig. 2. **a**, ATR-FTIR spectra of PVA/SPOH-PAA film loaded with PAA-UCNPs. **b**, porous structure of the nanocomposite film obtained with SEM InLens mode. **c**, Distribution of PAA-UCNPs (white spots) in the nanocomposite film obtained with SEM ESB mode. Scale bar: 200 nm.

the one at 443 °C is related to the degradation of PVA (breakdown of the polymer backbone) [33], SPOH (decomposition of polymer main chain) [34,35] and PAA (anhydride formation) [36]. The last weight loss at 759 °C was attributed to release of CO_2 from PAA component.

After the first heating cycle performed to reset the thermal history of the sample (dominated by an endothermal transition at 110 °C related to the loss of water), the DSC measurements (*Fig. S15*) revealed a transition at 94 °C attributable to the T_g of PAA component of the film and another

transition at 165 °C ascribable to anhydride formation from PAA [37]. Another transition was detected at 215 °C, which was attributed to the onset of PVA melting transition [38,39] together with the degradation of PAA anhydride [37] and the T_g of SPOH [40].

3.2. Hydrogen peroxide generation ability under solar irradiation

Subsequently, irradiation tests using a solar simulator were performed to determine the nanocomposite ability to generate H_2O_2 (Fig. 3 *a*). Control experiments in the absence of UCNPs were performed as well, achieving a 0.73 μM H_2O_2 concentration after 5 min, which did not change up to 120 min irradiation (*Table S4*). This behavior indicated that the polymer matrix itself presented a poor ability to generate H_2O_2 under artificial solar light irradiation. On the other hand, H_2O_2 concentration linearly increased in the presence of the nanocomposite, yielding a 9.3 μM H_2O_2 concentration after 120 min irradiation. These results proved the ability of the nanocomposite to operate under artificial solar light irradiation.

3.3. Photophysical operating mechanism

Following the results obtained from the photoinduced H_2O_2 generation experiments, photophysical investigations were conducted to elucidate the operating mechanism of the prepared nanocomposite. The upconversion emission spectra of the UCNPs and of the nanocomposite exhibited the typical emission bands of Tm^{3+} ions (Fig. 3 *b*), whose emission is sensitized via energy transfer upconversion (ETU) processes [41] from excited Yb^{3+} ions (Fig. 3 *c*). Upon irradiation at 980 nm, Yb^{3+}-Tm^{3+} co-doped UCNPs exhibited emission lines in the UV range (345 nm, $^1I_6 \rightarrow {}^3F_4$; 362 nm, $^1D_2 \rightarrow {}^3H_6$), in the visible range (474 nm, $^1G_4 \rightarrow {}^3H_6$; 644 nm, $^1G_4 \rightarrow {}^3F_4$; 694 nm, $^3F_3 \rightarrow {}^3H_6$) and in the NIR range (803 nm, $^3H_4 \rightarrow {}^3H_6$) [42]. The bands at 803 and 694 nm, originating from a

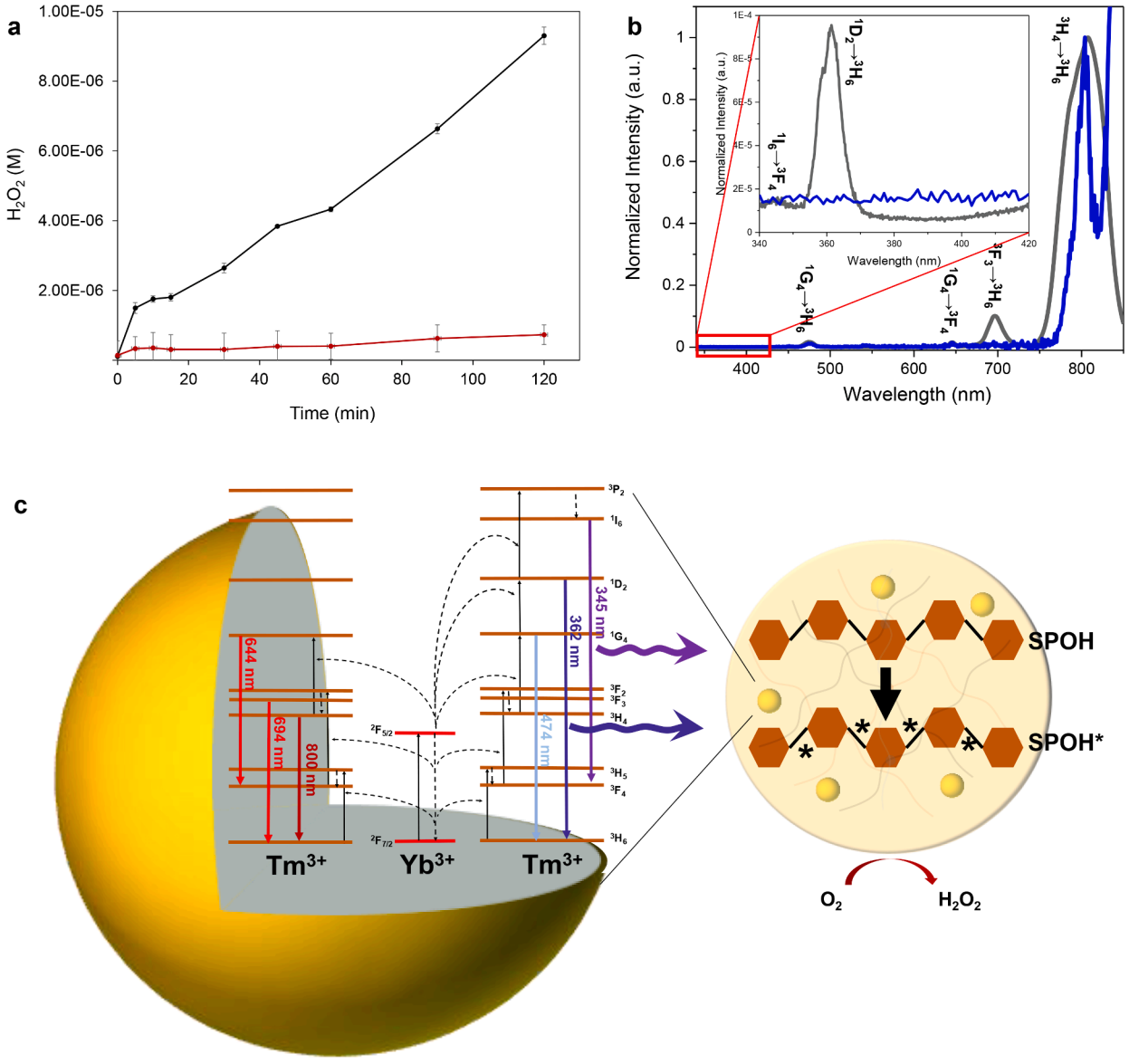

Fig. 3. **A**, Hydrogen peroxide production of PAA-UCNP-embedded PVA/SPOH-PAA film (black line) and of PVA/SPOH-PAA matrix (red line). The samples were put under simulated solar irradiation for 120 min. Reported values are the mean of 3 replicates. **b**, UC emission spectra of the β-$NaYF_4$:Yb^{3+}/Tm^{3+} (20/2%) UCNPs (black line) and the UCNP-embedded PVA/SPOH-PAA nanocomposite (blue line) upon 980 nm excitation. The spectra are normalized at Tm^{3+} emission at 803 nm. Inset shows the UC emission spectra in the wavelength range 340–420 nm. **c**, Schematic illustration of energy transfer processes between Yb^{3+}-Tm^{3+} co-doped UCNPs and PVA/SPOH-PAA nanocomposite upon 980 nm irradiation. (For interpretation of the references to colour in this figure legend, the reader is referred to the web version of this article.)

two-photon process, dominate the spectra because of the higher efficiency of two-photon upconversion emissions. The emissions at 644 nm and 474 nm are due to three-photon upconversion processes, while the emissions at 362 nm and 345 nm stem from a four-photon and a five-photon process, respectively [41].

Differently from UCNPs, the emission spectra of the nanocomposite lacked the bands at 345 and 362 nm, which indicates that the excitation energy of the relevant transitions $^1D_2 \rightarrow {}^3H_6$ and $^1I_6 \rightarrow {}^3F_4$ was transferred via non-radiative energy transfer processes to the benzophenone groups of SPOH, which are able to absorb light of similar energies[17]. The energy transfer processes lead to the sensitization of the triplet excited state of benzophenone group present in SPOH, which is responsible for the subsequent production of hydrogen peroxide, as discussed by Lockhart *et al.* [17] (Fig. 3 *c*).

Moreover, the band at 694 nm was not detected in the spectra of the nanocomposite: this could be ascribed to cross-relaxation processes occurring in the polymer matrix ($^3F_3 \rightarrow {}^3H_5$; $^3H_6 \rightarrow {}^3H_5$), leading to the population of $^3H_5$ [43].

3.4. Adsorption and photodegradation ability towards CIP

Ciprofloxacin (CIP) is a persistent antibiotic usually found in relatively high concentration in hospital wastewater and also present in drinking water [44]. As one of the most common antibiotics of the fluoroquinolone family, it was chosen to test the adsorption and the photodegradation ability of the nanocomposite.

Samples of the nanocomposite and the polymer matrix without UCNPs were put respectively in 100 mL of a 100 mg/L CIP aqueous solution for 150 min. The polymer matrix adsorbed 89.78 % of CIP, similarly to the nanocomposite (87.15 %) (*Fig. S13a*). These results proved that the polymer film could adsorb CIP effectively, and that the addition of UCNPs had a negligible effect on its adsorption capacity. The high porosity of the film (cf. Fig. 2 *b*) allowed an effective contact with the CIP solution. The adsorption processes were considered to be driven by the electrostatic interaction between PAA free carboxylate groups and CIP molecules: in the experimental pH conditions (6.5), CIP exists as zwitterion with protonated amine and deprotonated carboxylic groups (pK_a values 5.9 and 8.9) [45], while PAA is in its deprotonated form (pK_a 4.28) [29].

Adsorption kinetics were fitted using the intraparticle diffusion model [46].

$$q_t = k_p\sqrt{t} + C \tag{7}$$

where q_t (mg·g^{-1}) is the adsorption capacity, k_p (mg·g^{-1}·min$^{-0.5}$) is the adsorption rate constant and C (mg/g^{-1}) is the boundary layer thickness.

A relatively faster film diffusion (k_1; the adsorptive diffuses from the boundary layer to the exterior surface of the adsorbent) was followed by a 5.8-fold slower pore diffusion process (k_2, the adsorptive reaches the surface of the adsorbent and diffuses into the pores), followed in turn by a 3.2 slower adsorption process (k_3) (Fig. 4 *a*) [47]. The performance of the nanocomposite resulted better than the one of other widely used porous adsorbents [48], which were used in the adsorption of CIP under similar conditions and fitted with the intra-particle diffusion model (*Table S5*).

After reaching the adsorption–desorption equilibrium in 150 min, the same samples were irradiated with artificial solar light (*Figs. S5 and S12*). A negligible degradation of CIP was detected in the absence of the film (0.006 %) and in the presence of the film not containing UCNPs (0.19 %) during a 240 min irradiation, while CIP concentration was reduced to 50 % in the presence of the nanocomposite in the same irradiation period (*Fig. S13b*). These results confirmed the role played by the UCNPs in the photodegradation of CIP under artificial solar light.

More in detail, in the absence of the film and upon irradiation, the photolysis of CIP takes place, indicating that only the interaction between the artificial solar light and CIP drives the degradation. Photolysis of CIP in these experimental conditions is negligible and the same is valid in the presence of the polymer matrix in the absence of UCNPs (Fig S5). This is due to the fact that the artificial solar light used in the reported experiments lacks the UV component, which is energetic enough to directly degrade CIP. The removal of UV component from the light source was applied to be able to detect the photocatalytic effect of the nanocomposite, without the photolytic contribution of UV light.

In the presence of the nanocomposite, the UCNPs absorb the NIR component of the light source and upconvert it reaching higher energy excited states of Tm^{3+}. Subsequently, this excitation energy is transferred to SPEEK, resulting in the nonradiative deactivation of Tm^{3+} ions and the formation of SPEEK (n,π*) singlet excited state. After intersystem crossing to SPEEK (n,π*) triplet excite state, the latter abstracts a hydrogen atom from PVA, generating two radicals (one of PVA and one of SPEEK). These radicals react with dissolved oxygen to form peroxides, which finally evolve to produce H_2O_2 [17].

Surprisingly, it was not possible to obtain an accurate fit of the photodegradation kinetics with pseudo- zero, first and second order models. Therefore, the data were fitted using the intraparticle-diffusion model, which yielded a degradation rate constant equal to 3.49·10^{-2} mg·g^{-1}·min$^{-0.5}$ (Fig. 4 *b*). This suggested the occurrence of relatively faster photodegradation reactions coupled with a slower adsorption process. A possible mechanism is here proposed: i) H_2O_2 is photogenerated inside the film pores and reacts with the adsorbed CIP; ii) subsequently, the photodegradation products diffuse out of the film, freeing the active sites for new CIP molecules, which diffuse inside the

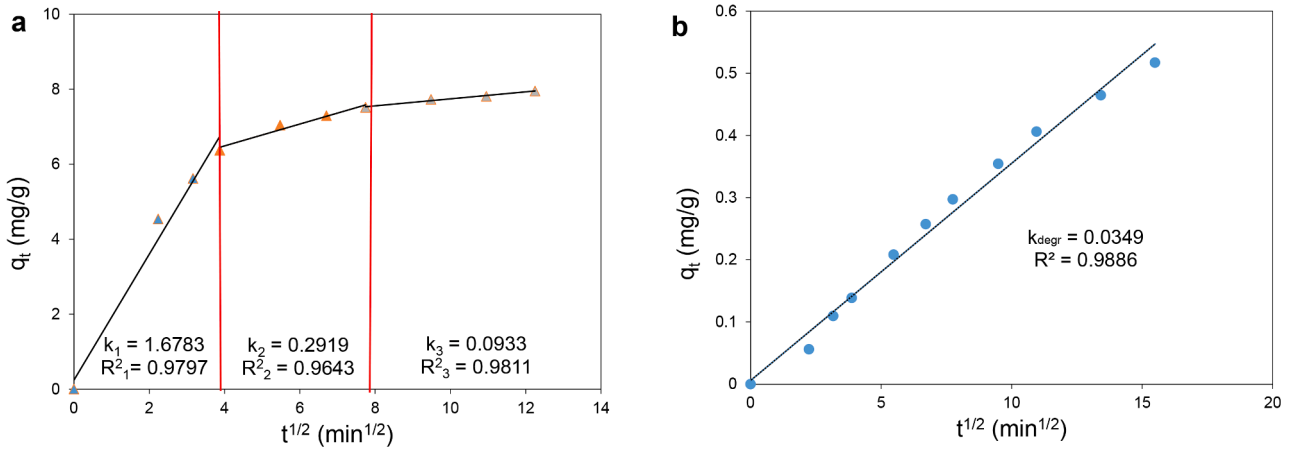

Fig. 4. A, Adsorption kinetic curve of CIP (100 mL of 100 mg/L, pH = 6.5) onto PAA-UCNP-embedded PVA/SPOH-PAA film and fitting with the intraparticle diffusion model. **b**, Intraparticle diffusion model fitting for CIP degradation kinetics by PAA-UCNP-embedded PVA/SPOH-PAA film.

nanocomposite film according to the intra-particle diffusion model.

3.5. Reusability and stability tests

For in-field applications, the assessment of the reusability and the stability of a photocatalyst is extremely important. Therefore, the stability of the nanocomposite was monitored for a period of 1 month via ICP-MS measurements (Fig. 5 *a*), revealing that more than 99% of the UCNPs remained entrapped in the polymer matrix in this time frame. This underlined the efficiency of the crosslinking step, which protects the UCNPs from leaching. UV–Vis analyses were as well conducted to monitor the stability of the polymeric components of the nanocomposite (Fig. 5 *b*), The results confirmed that the leaching of SPOH or PVA after 24 h immersion in water was non-significant.

The nanocomposite film was recovered and reused up to 3 cycles for CIP adsorption and degradation. A negligible variation of the adsorption capacity was detected over the cycles (88%, 87% and 90% for 1st, 2nd and 3rd cycle, respectively; Fig. 5 *c*) for the regenerated films. On the other hand, the reuse of a sample on which the regeneration process was not performed reduced its adsorption capacity to 47 %. As for the photodegradation experiments, a negligible reduction of the photocatalytic activity after 3 cycles was detected (52%, 54%, 51% for 1st, 2nd and 3rd cycle, respectively; Fig. 5 *d*). These results demonstrated the excellent stability and reusability of the nanocomposite for CIP concurrent adsorption and photodegradation.

To date, the NIR-induced photodegradation of CIP has not been reported in the literature and it is here first reported to the best of the authors' knowledge. The results of the present research work were then compared with the most recent studies on visible photocatalysis (*Table S6*). Tang *et al.* demonstrated that, in the presence of $Cu_{0.84}Bi_{2.08}O_4$/PDS (PDS = peroxydisulfate) and under visible irradiation, a 95% degradation of a 40 mg/mL CIP solution was obtained in 400 min. The non-regenerated catalyst suffered from the decreased degradation activity with the increase of the number of recycling steps. The photocatalyst material was therefore regenerated by washing and reused for only one cycle [49]. Wu *et al.* demonstrated that in the presence of montmorillonite under visible irradiation, a 70% degradation of a 210 mg/L CIP solution was obtained in 300 min. The reusability of the photocatalysts was not reported [50,51]. Sha *et al.* demonstrated that in the presence of Cu^{2+}/g-C_3N_4 under visible irradiation, a 70% degradation of CIP 8 mg/L solution was obtained in 60 min. The reusability of the photocatalysts was not reported [52].

In summary, the photocatalyst proposed in this work can be activated by NIR irradiation with good photodegradation efficiency towards CIP, which represents an alternative to visible-responsive photocatalysts in terms of a sustainable use of energy. Besides, the nanocomposite proposed in this research work can be recycled at least for 3 cycles without deteriorating its photocatalytic performance, differently from

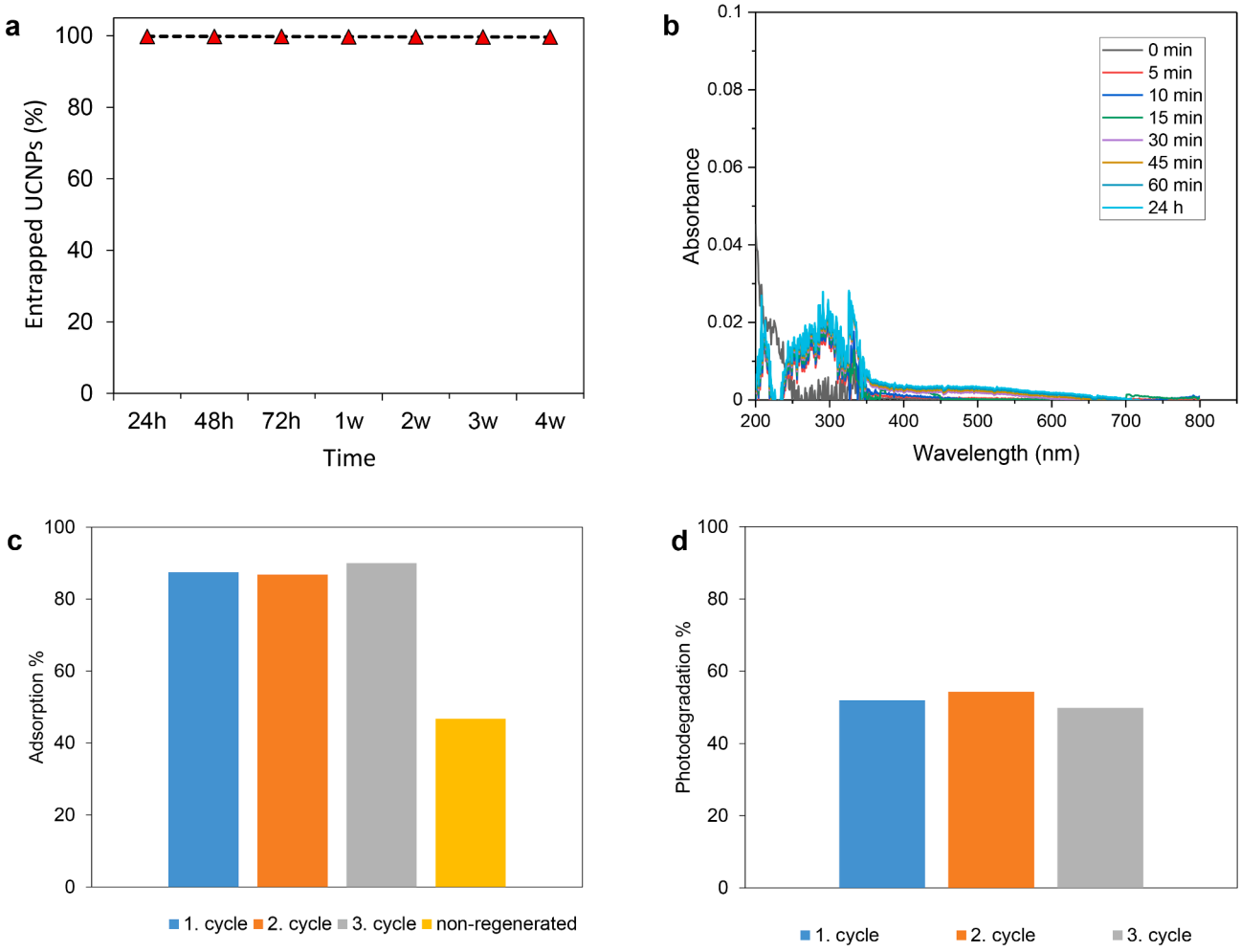

Fig. 5. **a**, Percentage of entrapped PAA-UCNPs in PAA-crosslinked nanocomposite immersed in ultrapure water in the time range from 24 h to 4 weeks. The data were collected via ICP-MS analyses of the amount of Y, Yb and Tm species present in water. Reported values are the mean of 3 replicates. **b**, UV–vis spectrum of the supernatant from water in contact with PVA/SPOH-PAA polymer film. **c**, CIP adsorption percentage of PAA-UCNP-embedded PVA/SPOH-PAA film up to 3 cycles, compared with the non-regenerated film. **d**, CIP degradation percentage of PAA-UCNP-embedded PVA/SPOH-PAA film up to 3 cycles.

the reported studies on visible photocatalysts. Despite the fact that the photocatalysts mentioned in *Table S6* exhibit higher efficiency for CIP photodegradation, a direct comparison cannot be performed since irradiance values are not reported in the above-mentioned studies.

3.6. Antibacterial activity tests

Antibacterial tests were performed to determine the bactericidal efficiency of the nanocomposite. A 8.9–15.7% bactericidal effect in the absence of the nanocomposite (Fig. 6 *a*) could be observed during 1 h solar irradiation compared to the samples in the absence of light. Similar results were obtained in the presence of the polymer matrix without UCNPs.

(9.8–14.4%). Conversely, a 47.3–55.2% bactericidal effect was registered in the presence of the nanocomposite, resulting thus 4 times higher with respect to the two previous experiments. In the absence of the nanocomposite as well as in the presence of the polymeric matrix without UCNPs, the bactericidal rate constant did not vary ($1.9{\cdot}10^{-3}$ min^{-1}), while in the presence of the nanocomposite a 4-fold increase was observed ($8.1{\cdot}10^{-3}$ min^{-1}) (Fig. 6 *b*).

The influence of the different experimental conditions was also investigated through monitoring the growth behavior of *E. coli* (Fig. 6 *c*). The bactericidal effect on *E. coli* for the samples in the absence of nanocomposite did not vary significantly with respect to the one in the presence of the polymer matrix without UCNPs, inducing a 17.7% and 22.6% decrease in optical density, respectively, with respect to the reference sample in dark conditions. According to previous studies, both solar light and H_2O_2 have lethal effect on *E. coli* [53,54]. The UV solar photons can activate the polymeric matrix in the absence of UCNPs to a limited extent and this accounted for the production of limited amounts of H_2O_2 in the *E. coli* suspension. Conversely, the growth of *E. coli* in the presence of the nanocomposite was drastically inhibited by 80%. The synergistic action of H_2O_2 and solar light was considered to be the cause for the higher inactivation of *E. coli* cells during cell culture and thus for the lower final optical density compared to the samples in the absence of the nanocomposite. These results again confirmed again the role of UCNPs in the production of H_2O_2.

4. Conclusions

In this work, we demonstrated that the PAA-UCNPs incorporated in a PVA/SPOH-PAA matrix via a simple crosslinking reaction constitute an efficient multifunctional material able to produce H_2O_2 under solar irradiation, thanks to photon upconversion and non-radiative energy transfer processes occurring between the UCNPs and the SPOH component. This nanocomposite was able to concurrently adsorb (87%) and photodegrade (50%) the antibiotic CIP, keeping its performance over 3 cycles. Furthermore, the nanocomposite was able to inhibit *E. coli* with a 80% bactericidal efficiency under solar irradiation.

The prepared nanocomposite presents a variety of advantages: (a)

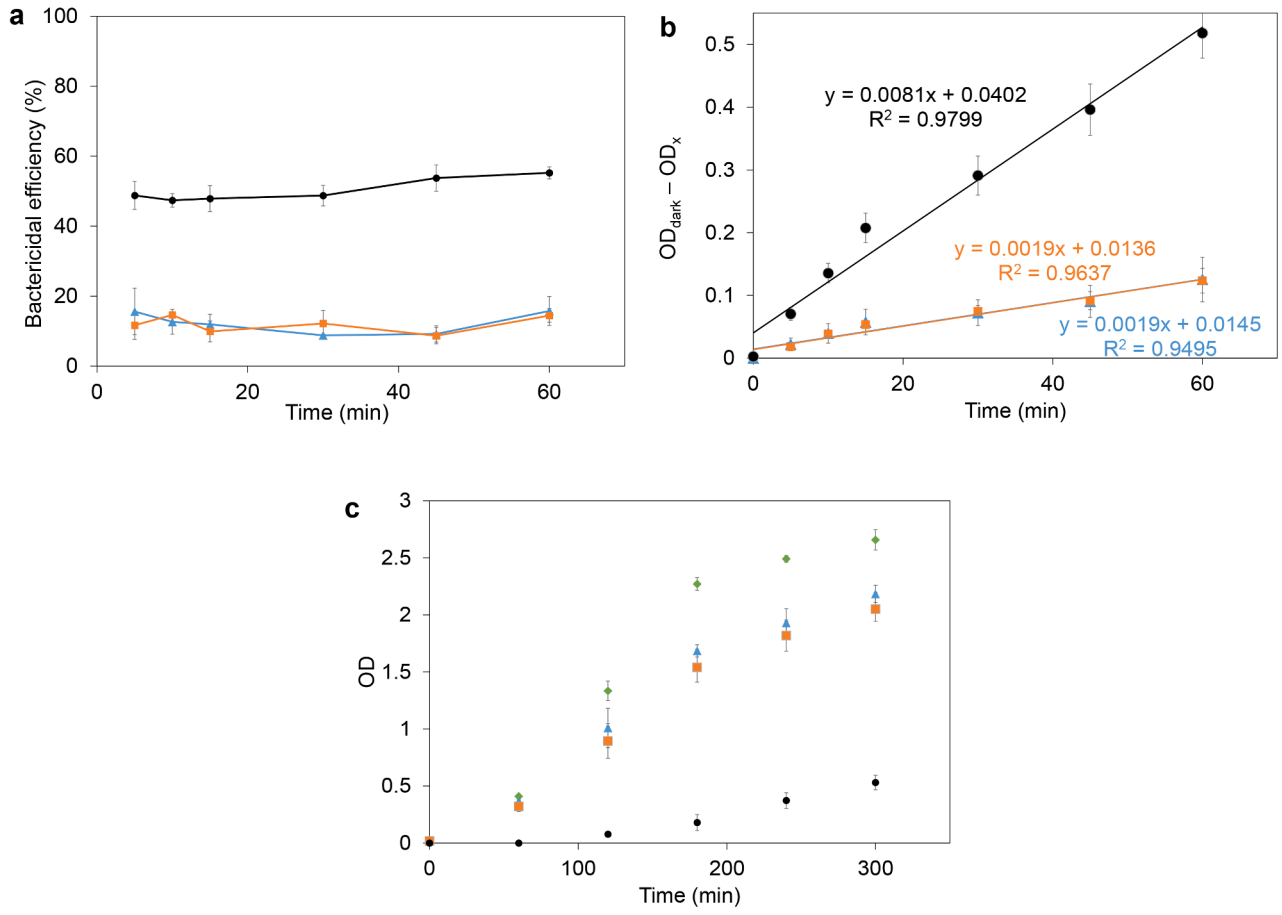

Fig. 6. **A**, Time-dependent variation of bactericidal efficiency towards *E. coli* under solar irradiation for different treatments: in the absence of the nanocomposite (blue line); in the presence of the polymer matrix without UCNPs (orange line); in the presence of the nanocomposite (black line). **b**, Photodegradation kinetics of *E. coli* under solar irradiation for different treatments: in the absence of the nanocomposite (blue line); in the presence of the polymer matrix without UCNPs (orange line); in the presence of the nanocomposite (black line). **c**, Time-dependent variation of optical density of *E. coli* during incubation at 37 °C for 300 min for different treatments: reference sample in dark conditions (green diamonds); upon irradiation in the absence of the nanocomposite (blue triangles), in the presence of the polymer matrix without UCNPs (orange squares), in the presence of the nanocomposite (black dots). (For interpretation of the references to colour in this figure legend, the reader is referred to the web version of this article.)

the non-leaching ability of the nanocomposite ensures the reuse of the photocatalyst and avoids secondary pollution upon use; (b) the use of solar light to activate the nanocomposite allows the operations to be independent from artificial irradiation sources, minimizing the consumption of energy; (c) the removal of pollutants can be performed under ambient conditions. Altogether, the results presented here contribute to demonstrate the possible application of this multifunctional nanocomposite for a solar-driven wastewater treatment process based on upconverting nanoparticles.

Declaration of Competing Interest

The authors declare that they have no known competing financial interests or personal relationships that could have appeared to influence the work reported in this paper.

Data availability

Data will be made available on request.

Acknowledgments

S.F. gratefully acknowledge financial support by the China Scholarship Council (CSC, 201908080207). M.S., N.L. and G.C. acknowledge financial support by the European Union's Horizon 2020 Research and Innovation Program under the Marie Sklodowska-Curie Grant Agreement No. 734381 (CARBO-IMmap) and No. 813036 (ULTIMATE), and support from Dresden Center for Nanoanalysis (DCN) of TU Dresden. M. G. gratefully acknowledges Ca' Foscari University FPI 2019 grant. S.F. thanks Dr. Xinne Zhao and Dr. Bergoi Ibarlucea for providing *E. coli*, Mrs. Sabrina Beutner for providing ICP-MS measurements, Mrs. Madlen Matterna for providing training of UCNPs synthesis and DLS measurements, Dr. Jiao Wang for providing training of photocatalysis experiments, Dr. Markus Löffler for providing training of SEM, Dr. Darius Pohl for providing training of TEM.

Author contribution

M.S., T.J., N.L. and G.C. initiated and supervised the project. J.E.I.J. and S.F. performed the experiments and data analysis. E.T. performed the photoluminescence measurements. M.G. performed TGA and DSC measurements. All authors extensively discussed the data. S.F., M.S. and T.J. wrote the paper.

Appendix A. Supplementary data

Supplementary data to this article can be found online at https://doi.org/10.1016/j.cej.2023.146877.

References

[1] R. Droste, R.L. Gehr, Theory and Practice of Water and Wastewater Treatment, 2nd ed., J. Wiley, New York, 2019.
[2] C. Grandclément, I. Seyssiecq, A. Piram, P. Wong-Wah-Chung, G. Vanot, N. Tiliacos, N. Roche, P. Doumenq, From the conventional biological wastewater treatment to hybrid processes, the evaluation of organic micropollutant removal: a review, Water Res. 111 (2017) 297–317, https://doi.org/10.1016/j.watres.2017.01.005.
[3] Y. Luo, W. Guo, H.H. Ngo, L.D. Nghiem, F.I. Hai, J. Zhang, S. Liang, X.C. Wang, A review on the occurrence of micropollutants in the aquatic environment and their fate and removal during wastewater treatment, Sci. Total Environ. 473–474 (2014) 619–641, https://doi.org/10.1016/j.scitotenv.2013.12.065.
[4] S. Malato, P. Fernández-Ibáñez, M.I. Maldonado, J. Blanco, W. Gernjak, Decontamination and disinfection of water by solar photocatalysis: recent overview and trends, Catal. Today 147 (1) (2009) 1–59, https://doi.org/10.1016/j.cattod.2009.06.018.
[5] D.B. Miklos, C. Remy, M. Jekel, K.G. Linden, J.E. Drewes, U. Hübner, Evaluation of advanced oxidation processes for water and wastewater treatment – a critical review, Water Res. 139 (2018) 118–131, https://doi.org/10.1016/j.watres.2018.03.042.
[6] M.A. Oturan, J.-J. Aaron, Advanced oxidation processes in water/wastewater treatment: principles and applications. a review, Crit. Rev. Environ. Sci. Technol. 44 (23) (2014) 2577–2641, https://doi.org/10.1080/10643389.2013.829765.
[7] K. Rajeshwar, M.E. Osugi, W. Chanmanee, C.R. Chenthamarakshan, M.V.B. Zanoni, P. Kajitvichyanukul, R. Krishnan-Ayer, Heterogeneous photocatalytic treatment of organic dyes in air and aqueous media, J Photochem Photobiol C: Photochem Rev 9 (4) (2008) 171–192, https://doi.org/10.1016/j.jphotochemrev.2008.09.001.
[8] Z. Li, Z. Li, C. Zuo, X. Fang, Application of nanostructured TiO2 in UV photodetectors: a review, Adv. Mater. 34 (28) (2022) 2109083, https://doi.org/10.1002/adma.202109083.
[9] J. Wang, L. Svoboda, Z. Němečková, M. Sgarzi, J. Henych, N. Licciardello, G. Cuniberti, Enhanced Visible-Light Photodegradation of Fluoroquinolone-Based Antibiotics and *E. Coli* Growth Inhibition Using Ag–TiO $_2$ Nanoparticles, RSC Adv. 11 (23) (2021) 13980–13991, https://doi.org/10.1039/D0RA10403E.
[10] C. Jia, X. Zhang, K. Matras-Postolek, B. Huang, P. Yang, Z-Scheme reduced graphene oxide/TiO2-bronze/W18O49 ternary heterostructure towards efficient full solar-spectrum photocatalysis, Carbon 139 (2018) 415–426, https://doi.org/10.1016/j.carbon.2018.07.024.
[11] N.A. Almeida, P.M. Martins, S. Teixeira, J.A. Lopes da Silva, V. Sencadas, K. Kühn, G. Cuniberti, S. Lanceros-Mendez, P.A.A.P. Marques, TiO2/Graphene oxide immobilized in P(VDF-TrFE) electrospun membranes with enhanced visible-light-induced photocatalytic performance, J. Mater. Sci. 51 (14) (2016) 6974–6986, https://doi.org/10.1007/s10853-016-9986-4.
[12] J. Wang, M. Sgarzi, Z. Němečková, J. Henych, N. Licciardello, G. Cuniberti, Reusable and antibacterial polymer-based nanocomposites for the adsorption of dyes and the visible-light-driven photocatalytic degradation of antibiotics, Glob. Chall. 6 (11) (2022) 1–11, https://doi.org/10.1002/gch2.202200076.
[13] M.M. Falinski, R.S. Turley, J. Kidd, A.W. Lounsbury, M. Lanzarini-Lopes, A. Backhaus, H.E. Rudel, M.K.M. Lane, C.L. Fausey, A.C. Barrios, J.E. Loyo-Rosales, F. Perreault, W.S. Walker, L.B. Stadler, M. Elimelech, J.L. Gardea-Torresdey, P. Westerhoff, J.B. Zimmerman, Doing nano-enabled water treatment right: sustainability considerations from design and research through development and implementation, Environ. Sci. Nano 7 (11) (2020) 3255–3278, https://doi.org/10.1039/D0EN00584C.
[14] A.V. Baskar, N. Bolan, S.A. Hoang, P. Sooriyakumar, M. Kumar, L. Singh, T. Jasemizad, L.P. Padhye, G. Singh, A. Vinu, B. Sarkar, M.B. Kirkham, J. Rinklebe, S. Wang, H. Wang, R. Balasubramanian, K.H.M. Siddique, Recovery, regeneration and sustainable management of spent adsorbents from wastewater treatment streams: a review, Sci. Total Environ. 822 (2022), 153555, https://doi.org/10.1016/j.scitotenv.2022.153555.
[15] H. Syahirah Zakria, M.H. Dzarfan Othman, R. Kamaludin, S.H.S.A. Kadir, T. Agustiono Kurniawan, A. Jilani, Immobilization techniques of a photocatalyst into and onto a polymer membrane for photocatalytic activity, RSC Adv. 11 (12) (2021) 6985–7014, https://doi.org/10.1039/D0RA10964A.
[16] Z. Abousalman-Rezvani, H. Roghani-Mamaqani, H. Riazi, O. Abousalman-Rezvani, Water treatment using stimuli-responsive polymers, Polym. Chem. 13 (42) (2022) 5940–5964, https://doi.org/10.1039/D2PY00992G.
[17] P. Lockhart, B.K. Little, B.L. Slaten, G. Mills, Photogeneration of H2O2 in water-swollen SPEEK/PVA polymer films, J. Phys. Chem. A 120 (22) (2016) 3867–3877, https://doi.org/10.1021/acs.jpca.6b00442.
[18] B.K. Little, P. Lockhart, B.L. Slaten, G. Mills, Photogeneration of H2O2 in SPEEK/PVA aqueous polymer solutions, Chem. A Eur. J. 117 (20) (2013) 4148–4157, https://doi.org/10.1021/jp4021728.
[19] P. Devi, U. Das, A.K. Dalai, In-situ chemical oxidation: principle and applications of peroxide and persulfate treatments in wastewater systems, Sci. Total Environ. 571 (2016) 643–657, https://doi.org/10.1016/j.scitotenv.2016.07.032.
[20] B. Bharti, H. Li, Z. Ren, R. Zhu, Z. Zhu, Recent advances in sterilization and disinfection technology: a review, Chemosphere 308 (2022), 136404, https://doi.org/10.1016/j.chemosphere.2022.136404.
[21] M. Haase, H. Schäfer, Upconverting nanoparticles, Angew. Chem. Int. Ed. 50 (26) (2011) 5808–5829, https://doi.org/10.1002/anie.201005159.
[22] F.M. Pennisi, A.L. Pellegrino, N. Licciardello, C. Mezzalira, M. Sgarzi, A. Speghini, G. Malandrino, G. Cuniberti, Synthesis, characterization and photocatalytic properties of nanostructured lanthanide doped β-nayf4/tio2 composite films, Sci. Rep. 12 (1) (2022) 1–11, https://doi.org/10.1038/s41598-022-17256-2.
[23] J. Xue, M. Sheng, G. Wu, Y. Liu, L. Shi, Q. Bi, NIR to intense UV-blue photon transition by upconverting LuF3: Yb3+, Tm3+@BiOCl core@shell composite for pollutant degradation, J. Alloy. Compd. 959 (2023), 170519, https://doi.org/10.1016/j.jallcom.2023.170519.
[24] P. Xing, G.P. Robertson, M.D. Guiver, S.D. Mikhailenko, K. Wang, S. Kaliaguine, Synthesis and characterization of sulfonated poly(ether ether ketone) for proton exchange membranes, J. Membr. Sci. 229 (1–2) (2004) 95–106, https://doi.org/10.1016/j.memsci.2003.09.019.
[25] S. Feng, Y. Shang, Y. Wang, G. Liu, X. Xie, W. Dong, J. Xu, V.K. Mathur, Synthesis and crosslinking of hydroxyl-functionalized sulfonated poly(ether ether ketone) copolymer as candidates for proton exchange membranes, J. Membr. Sci. 352 (1–2) (2010) 14–21, https://doi.org/10.1016/j.memsci.2010.01.040.
[26] A. Nsubuga, M. Sgarzi, K. Zarschler, M. Kubeil, R. Hübner, R. Steudtner, B. Graham, T. Joshi, H. Stephan, Facile preparation of multifunctionalisable "stealth" upconverting nanoparticles for biomedical applications, Dalton Trans. 47 (26) (2018) 8595–8604, https://doi.org/10.1039/c8dt00241j.
[27] J. Hesse, D.T. Klier, M. Sgarzi, A. Nsubuga, C. Bauer, J. Grenzer, R. Hübner, M. Wislicenus, T. Joshi, M.U. Kumke, H. Stephan, Rapid synthesis of sub-10 Nm hexagonal NaYF4-based upconverting nanoparticles using therminol® 66, ChemistryOpen 7 (2) (2018) 159–168, https://doi.org/10.1002/open.201700186.

[28] S.F. Himmelstoß, T. Hirsch, Long-term colloidal and chemical stability in aqueous media of NaYF4-Type upconversion nanoparticles modified by ligand-exchange, Part. Part. Syst. Char. 36 (10) (2019), https://doi.org/10.1002/ppsc.201900235.
[29] F. Jianqi, G. Lixia, PVA/PAA Thermo-crosslinking hydrogel fiber: preparation and ph-sensitive properties in electrolyte solution, Eur. Polym. J. 38 (8) (2002) 1653–1658, https://doi.org/10.1016/S0014-3057(02)00032-0.
[30] K. Kumeta, I. Nagashima, S. Matsui, K. Mizoguchi, Crosslinking reaction of poly (Vinyl Alcohol) with poly(Acrylic Acid) (PAA) by heat treatment: effect of neutralization of PAA, J. Appl. Polym. Sci. 90 (9) (2003) 2420–2427, https://doi.org/10.1002/app.12910.
[31] A.I. Caço, F. Varanda, M.J. Pratas de Melo, A.M.A. Dias, R. Dohrn, I.M. Marrucho, Solubility of antibiotics in different solvents. part ii. non-hydrochloride forms of tetracycline and ciprofloxacin, Ind. Eng. Chem. Res. 47 (21) (2008) 8083–8089, https://doi.org/10.1021/ie8003495.
[32] B.C. Smith, Infrared Spectral Interpretation : A Systematic Approach, 2nd edition, CRC Press, Boca Raton, 2018.
[33] B.J. Holland, J.N. Hay, The thermal degradation of poly(Vinyl Alcohol), Polymer 42 (16) (2001) 6775–6783, https://doi.org/10.1016/S0032-3861(01)00166-5.
[34] P. Knauth, H. Hou, E. Bloch, E. Sgreccia, M.L. Di Vona, Thermogravimetric analysis of SPEEK membranes: thermal stability, degree of sulfonation and cross-linking reaction, J. Anal. Appl. Pyrol. 92 (2) (2011) 361–365, https://doi.org/10.1016/j.jaap.2011.07.012.
[35] W. Li, J. Jiang, H. An, S. Dong, Z. Yue, H. Qian, H. Yang, Self-cross-linked sulfonated poly(ether ether ketone) with pendant sulfoalkoxy groups for proton exchange membrane fuel cells, ACS Appl. Energy Mater. 4 (3) (2021) 2732–2740, https://doi.org/10.1021/acsaem.1c00022.
[36] M.A. Moharram, M.G. Khafagi, Thermal behavior of poly(acrylic acid)–poly(vinyl pyrrolidone) and poly(acrylic acid)–metal–poly(vinyl pyrrolidone) complexes, J. Appl. Polym. Sci. 102 (4) (2006) 4049–4057, https://doi.org/10.1002/app.24367.
[37] J.J. Maurer, D.J. Eustace, C.T. Ratcliffe, Thermal characterization of poly(Acrylic Acid), Macromolecules 20 (1) (1987) 196–202, https://doi.org/10.1021/ma00167a035.
[38] S.R. Sudhamani, M.S. Prasad, K. Udaya Sankar, DSC and FTIR Studies on gellan and polyvinyl alcohol (PVA) Blend films, Food Hydrocoll. 17 (3) (2003) 245–250, https://doi.org/10.1016/S0268-005X(02)00057-7.
[39] G.M. Wu, S.J. Lin, C.C. Yang, Preparation and characterization of PVA/PAA membranes for solid polymer electrolytes, J. Membr. Sci. 275 (1) (2006) 127–133, https://doi.org/10.1016/j.memsci.2005.09.012.
[40] P. Xing, G.P. Robertson, M.D. Guiver, S.D. Mikhailenko, K. Wang, S. Kaliaguine, Synthesis and characterization of sulfonated poly(ether ether ketone) for proton exchange membranes, J. Membr. Sci. 229 (1) (2004) 95–106, https://doi.org/10.1016/j.memsci.2003.09.019.
[41] H. Dong, L.D. Sun, C.H. Yan, Energy transfer in lanthanide upconversion studies for extended optical applications, Chem. Soc. Rev. 44 (6) (2015) 1608–1634, https://doi.org/10.1039/c4cs00188e.
[42] F. Wang, X. Liu, Recent advances in the chemistry of lanthanide-doped upconversion nanocrystals, Chem. Soc. Rev. 38 (4) (2009) 976–989, https://doi.org/10.1039/b809132n.
[43] A. Nexha, Synthesis and Characterizations of Multifunctional Luminescent Lanthanide Doped (Doctoral dissertation), University of Rovira i Virgili, 2020.
[44] OECD, Pharmaceutical residues in freshwater : hazards and policy responses; OECD studies on water, OECD Publishing: Paris (2019).
[45] C.A. Igwegbe, S.N. Oba, C.O. Aniagor, A.G. Adeniyi, J.O. Ighalo, Adsorption of ciprofloxacin from water: a Comprehensive Review, J. Ind. Eng. Chem. 93 (2021) 57–77, https://doi.org/10.1016/j.jiec.2020.09.023.
[46] Kajjumba, William George, G.; Emik, S.; Öngen, A.; Kurtulus Özcan, H.; Aydın, S. Modelling of Adsorption Kinetic Processes—Errors, Theory and Application. *Adv. Sorpt. Process Appl.* **2019**, 1–19. https://doi.org/10.5772/intechopen.80495.
[47] H.N. Tran, S.J. You, A. Hosseini-Bandegharaei, H.P. Chao, Mistakes and inconsistencies regarding adsorption of contaminants from aqueous solutions: a critical review, Water Res. 120 (2017) 88–116, https://doi.org/10.1016/j.watres.2017.04.014.
[48] A. Avcı, İ. İnci, N. Baylan, A Comparative adsorption study with various adsorbents for the removal of ciprofloxacin hydrochloride from water, Water Air Soil Pollut. 230 (10) (2019), https://doi.org/10.1007/s11270-019-4315-6.
[49] H. Tang, Z. Dai, X. Xie, Z. Wen, R. Chen, Promotion of peroxydisulfate activation over Cu0.84Bi2.08O4 for visible light induced photodegradation of ciprofloxacin in water matrix, Chem. Eng. J. 356 (2019) 472–482, https://doi.org/10.1016/j.cej.2018.09.066.
[50] Q. Wu, Z. Que, Z. Li, S. Chen, W. Zhang, K. Yin, H. Hong, Photodegradation of ciprofloxacin adsorbed in the intracrystalline space of montmorillonite, J. Hazard. Mater. 359 (2018) 414–420, https://doi.org/10.1016/j.jhazmat.2018.07.041.
[51] F. Wu, J. Li, Z. Peng, N. Deng, Photochemical formation of hydroxyl radicals catalyzed by montmorillonite, Chemosphere 72 (3) (2008) 407–413, https://doi.org/10.1016/j.chemosphere.2008.02.034.
[52] J. Sha, L. Li, Z. An, M. He, H. Yu, Y. Wang, B. Gao, S. Xu, Diametrically opposite effect of Cu2+ on sulfamerazine and ciprofloxacin adsorption-photodegradation in g-C3N4/Visible light system: behavior and mechanism study, Chem. Eng. J. 428 (2022), 131065, https://doi.org/10.1016/j.cej.2021.131065.
[53] I. Barcina, I. Arana, J. Iriberri, L. Egea, Influence of light and natural microbiota of the butrón river on E Coli survival, Antonie Van Leeuwenhoek 52 (6) (1986) 555–566, https://doi.org/10.1007/BF00423416.
[54] B.J. Juven, M.D. Pierson, Antibacterial effects of hydrogen peroxide and methods for its detection and quantitation†, J. Food Prot. 59 (11) (1996) 1233–1241, https://doi.org/10.4315/0362-028X-59.11.1233.